Title: Giant Polarization in Super-Tetragonal Ferroelectric Thin Films through Interphase Strain

Authors: *Linxing Zhang,[1] Jun Chen,[1]* Longlong Fan,[1] Oswaldo Diéguez,[2] Jiangli Cao,[3] Zhao Pan,[1] Yilin Wang,[1] Jinguo Wang,[4] Moon Kim,[4] Shiqing Deng,[5] Jiaou Wang,[6] Huanhua Wang,[6] Jinxia Deng,[1] Ranbo Yu,[1] James F. Scott,[7] Xianran Xing[1]**

Affiliations:

[1] *Department of Physical Chemistry, University of Science and Technology Beijing, Beijing 100083, China E-mail: junchen@ustb.edu.cn, xing@ustb.edu.cn*

[2] *Department of Materials Science and Engineering, Faculty of Engineering; The Raymond and Beverly Sackler Center for Computational Molecular and Materials Science; Tel Aviv University, Tel Aviv 6997801, Israel*

[3] *Institute of Advanced Materials and Technology, University of Science and Technology Beijing, Beijing 100083, China*

[4] *Department of Materials Science and Engineering, University of Texas at Dallas, Richardson, Texas 75080, United States*

[5] *National Center for Electron Microscopy in Beijing, School of Materials Science and Engineering, The State Key Laboratory of New Ceramics and Fine Processing, Key Laboratory of Advanced Materials (MOE), Tsinghua University, Beijing 100084, People's Republic of China*

[6] *Institute of High Energy Physics, Chinese Academy of Sciences, Beijing 100049, China*

[7] *School of Chemistry and School of Physics, St Andrews University, St Andrews, Fife, Scotland*

**Correspondence to: junchen@ustb.edu.cn, xing@ustb.edu.cn.*

Abstract: Strain engineering has emerged as a powerful tool to create new states of known materials with excellent performance. Here, we show a general and practically realizable method via interphase strain to obtain a new super tetragonality providing giant polarization. This method is illustrated for the case of $PbTiO_3$, where we report a *c*/*a* ratio of up to 1.238 in epitaxial composite thin films, compared to that of 1.065 in bulk $PbTiO_3$. These thin films of super-tetragonal structure possess an unprecedented giant remanent polarization, 236.3 $\mu C/cm^2$, which is almost twice the value of all known ferroelectrics. The tetragonal phase is stable up to 725 °C as compared to the bulk's transition temperature of 490 °C. The present interphase strain approach could provide a new avenue to enhance the physical properties of materials with respect to their multiferroic, photonic, superconductor, and energy-harvesting behavior.

Main Text:

Strain offers a handle to enhance the properties of multifunctional materials (*1-3*), including magnetoresistance, superconductivity and ferroelectricity. For example, the critical temperature of the $La_{1.9}Sr_{0.1}CuO_4$ superconductor was raised from 25 K to 49.1 K using epitaxial strain (2). Another example concerns multiferroic $BiFeO_3$, whereby a large biaxial compressive strain in films changed their rhombohedral phase into a super-tetragonal one. Significantly different ferroelectric and antiferromagnetic properties have been achieved (*4*). Among strained ferroelectrics (*5-8*), widely studied perovskite oxides appearing with giant tetragonality may have a large value of the polarization and a high Curie temperature (T_C) as a consequence of their large dipolar moment (4,*9-12*), providing greatly added value for electronic device design. However, these compounds are rare and generally demand extreme synthesis conditions. One example of the synthetic approach to obtain such behavior is the expensive high compressive

pressure with diamond anvil cells (*11*,*12*), such as for preparation of $PbVO_3$ and $BiCoO_3$. Another approach of using the particular biaxial strain imposed by lattice-mismatched substrates on films has been successfully applied in many cases (1,*10*,*13*,*14*). It is also possible to use isotropic strain to affect the structure and properties of materials (*11*,*12*,*15*-*18*). The T_C of pulsed-laser deposition $BaTiO_3$ films can be controllably tuned to over 800 °C by the coupling between epitaxial strain and the isotropic strain provided by defect dipoles (*16*). In particular, it has been shown that isotropic tensile strain (negative pressure) theoretically increases tetragonality and polarization of perovskite oxides, such as $BaTiO_3$ and $PbTiO_3$ (fig. S1) (*15*). Experimentally, Wang et al. have successfully achieved a negative pressure in $PbTiO_3$ nanowires by taking advantage of the phase transformation induced stress to enhance physical properties (*17*,*18*). The isotropic strain is assuredly crucial for the design of materials; however, engineering such high negative pressure in experiments is regarded as a great challenge. A simpler practical approach for achieving the same effects as negative pressure is therefore desired, especially for epitaxial films.

Here, we investigate such concept, termed "interphase strain", to introduce large strain, in which two materials having similar crystal structure but different lattice parameters can be grown in a single epitaxial composite, so that the interfaces between them are matched coherently with similar lattice parameters. This is different to the conventional composite, in which different phases have their own lattice parameters. In this way an isotropic tensile or compression strain can be introduced into the material which originally had the smaller or larger lattice parameters, respectively. This strain is named interphase strain, and it can be expected to improve the structure and properties of functional materials. In this study this concept of interphase strain has been implemented to introduce a negative pressure in $PbTiO_3$ epitaxial composite ferroelectric

thin films via PbO. Our results feature a much larger polarization, *c*/*a* ratio, and stable temperature than any previous studies on $PbTiO_3$.

The epitaxial composite films were grown on $SrTiO_3$ (STO) substrates using a simple radio-frequency (rf) magnetron sputtering. The atomic deposition rate can be controlled by the oxygen ratio as discussed below. The samples of PT (I), and PT (II) were prepared without oxygen, and with 9 % oxygen, respectively. If either of PT (I) or PT (II) samples is annealed above 725°C, then a new atomic structure is obtained, classified as PI (III). Figure 1A highlights a small region (17° to 24°) of the general X-ray diffraction scans, demonstrating the apparent change in the *c* lattice parameters of PT (I), PT (II), and PT (III). Together with the results of high resolution X-ray scans covering a large angle (15° to 75°) (fig. S2A), only diffraction peaks from the directions of (100) STO substrate and (001) films can be observed. It reveals that all films are epitaxial and have a single set of tetragonal lattice parameter. Additional phi scans of both (101) and (103) planes of PT (I) feature four-axis symmetric structure, confirming an in-plane epitaxial relationship (Fig. 1C).

The typical epitaxial $PbTiO_3$ films (PT (III)) reveal the normal *c* lattice parameter of ~4.08 Å that is established in the literature (*19*). In contrast, the primitive PT (I) and PT (II) grown on the same STO substrate exhibit strong reflections at anomalous values corresponding to *c* lattice parameters of ~4.408 Å and ~4.840 Å, respectively. Subsequent synchrotron-based X-ray reciprocal space mappings (RSM) about the (103) plane of the films and substrates (Fig. 1B) verify that the *a* axis is well matched between the substrates and the films, but the *c* axis of the films unveil a colossal difference. The position of the *c* axis of bulk $PbTiO_3$ is indicated by the dotted line for comparison, which is similar to that of the normal coherently strained $PbTiO_3$ thin films (PT (III)). Strikingly, an increase in the *c* axis is observed in PT (I) and PT (II) by 16.5 %

and 6.1 %, respectively, as compared to the bulk value (*20*). Furthermore, both *c* and *c*/*a* increase with increasing thickness of PT (I) or PT (II) (Fig. 1D), which indicates that the growth strain is weakly controlled by the substrate as discussed in Table S1.

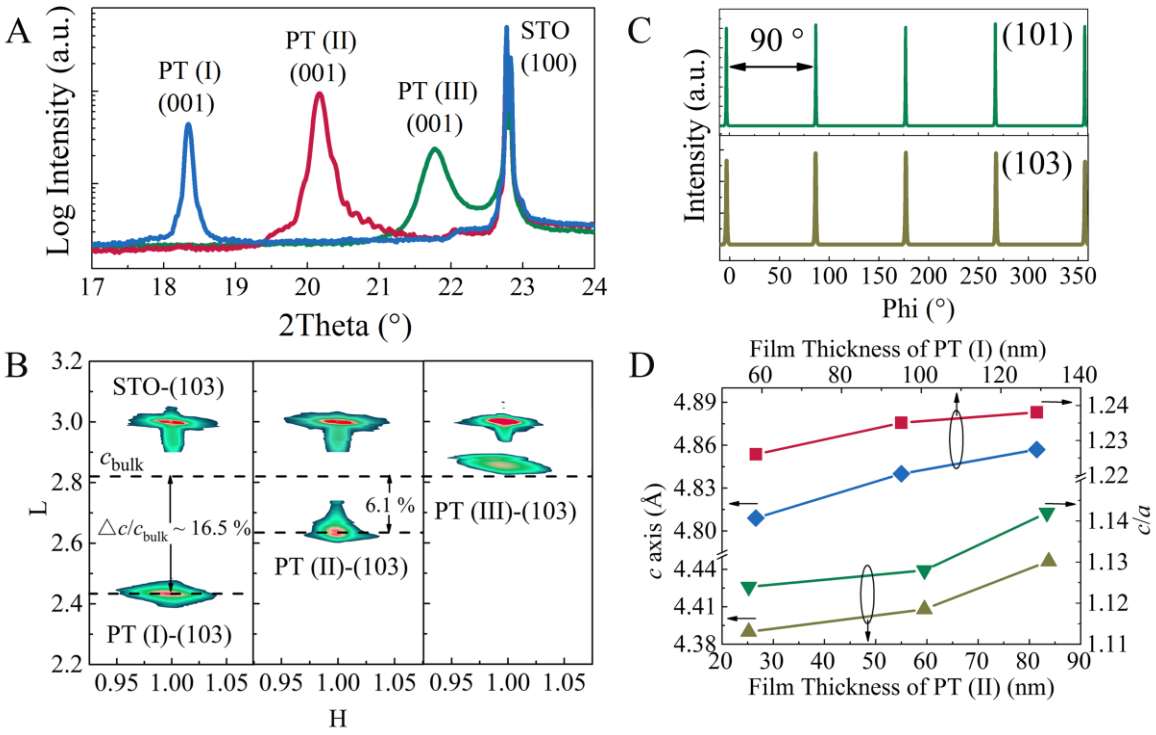

Fig. 1. Crystal structure characterization of epitaxial composite films. (**A**) Out-of-plane XRD of (001) peaks of PT (I), PT (II), and PT (III) epitaxial thin films on (100) STO substrates. (**B**) Synchrotron-based (103) X-ray RSM study of PT (I), PT (II), and PT (III) epitaxial thin films about the STO (103) diffraction condition. (**C**) The phi scans of both (101) and (103) planes of PT (I), demonstrating four-axis symmetric structure. (**D**) The lattice parameters of *c* and *c*/*a* of PT (I) and PT (II) as a function of thickness. The original data come from Table S1.

$PbTiO_3$ has a tetragonal perovskite structure with lattice parameters a = 3.899 Å, c = 4.154 Å, and c/a of 1.065 (Fig. 2A) (*20*). The precursor of PbO, which is used to prepare $PbTiO_3$, has a similar tetragonal structure, but with a large c/a ratio (a = 3.9729 Å, c = 5.0217 Å, c/a = 1.264) (Fig. 2B) (*21*). The perovskite-like periodic configuration can be identified in the plate-like PbO as marked by the red rectangular frame in Fig. 2B. The similarity in structure between the

$PbTiO_3$ and PbO configurations offers the potential for realizing the heteroepitaxial growth with interphase strain. Experimentally, in order to obtain such self-assembled heteroepitaxial composite films of the stretched $PbTiO_3$ with the compressed PbO, the atomic deposition rate has been controlled effectively for their different growth kinetics. Primarily, the Pb-rich composition determined by chemical analysis (ICP-OES) is uniform throughout the films detected by Auger electron spectroscopy with depth analysis (Fig. 2C), except for the higher Pb concentration on the surface. This verifies the homogeneous and randomly alternate growth of $PbTiO_3$ and PbO in both PT (I) and PT (II) (fig. S3). The dashed circles of Fig. 2D highlight different lattice configuration and contrast with their surroundings. The fast Fourier transform (FFT) pattern taken from a typical example of the regions marked by the dashed circles features a tetragonal structure but with an extinction of (100) plane. It reveals that these regions are PbO (Fig. 2F). However, the other surrounding regions provide a typical FFT pattern for the super-tetragonal $PbTiO_3$ structure (Fig. 2E). The results indicate that the metastable PbO is randomly distributed in $PbTiO_3$. The direct evidence for the heteroepitaxial structure between $PbTiO_3$ and PbO in the present PT (I) is provided by the spherical aberration-corrected high-angle annular-dark-field (HAADF) Z-contrast scanning transmission electron microscope (STEM) image (Fig. 2G). The bright, light grey, and dark grey contrast spots correspond to Pb (Z = 82, where Z is the atomic number), Sr (Z = 38), and Ti (Z = 22) columns, respectively, which is approximately proportional to Z^2 (6,*22*). The intensity profile along the red dashed line in Fig. 2H reveals a transition from Ti of $PbTiO_3$ to Pb of PbO, indicating a good lattice matching at the $PbTiO_3$/PbO interface (Fig. 2I). Both $PbTiO_3$ and PbO in PT (I) have the same *c* lattice parameter (4.840 Å) (Fig. 1 and 2G). Hence, in the present PT (I) epitaxial thin films PbO suffers a small out-of-plane compression strain of 3.6 %, while a giant tensile strain (16.5 %) for $PbTiO_3$ (Fig. 1B). It is

worth noting that the defect dipole generated in such special environment usually cannot produce such giant strain (*16*).

Investigations employing HAADF-STEM (*c*/*a* = 1.224) (Fig. 2) underpin the giant *c*/*a* ratio of $PbTiO_3$ in PT (I) (*c*/*a* = 1.238, Table S1) as determined from both macroscopic XRD and synchrotron-based RSM about the (103) plane (Fig. 1B). This *c*/*a* value is much larger than that of bulk (1.065), or in any other previously reported results for $PbTiO_3$ (*17*). It is comparable to that of the super-tetragonal phases that appear in the biaxial-strained $BiFeO_3$ films (1.232) and in those perovskite compounds synthesized by high-pressure and high-temperature methods, such as $PbVO_3$ (1.229), and $BiCoO_3$ (1.267) (*10*-*12*).

Intriguingly, the *c*/*a* ratio can be adjusted by controlling the oxygen ratio during the growth of thin films. For example, the sample PT (II) was prepared with 9 % oxygen, which features not only smaller *c*/*a* (1.142) but also lower Pb concentration than PT (I) (ICP-OES analysis in Materials and Methods, Fig. 1, fig. S3, and fig. S4). Therefore, the oxygen ratio affects the Pb atomic deposition rate of the $PbTiO_3$ epitaxial composite thin films. To grow the present super-tetragonal films, an atmosphere with deficient oxygen is required for fast PbO nucleation. The volume fractions of $PbTiO_3$ and PbO are 100/0, 80/20, and 45.3/54.7 for the PT (III), PT (II) and PT (I) thin films, respectively. The amount of PbO in the present films determines the *c*/*a* ratio, which further reveals the role of PbO in interphase strain (fig. S22). It is important to note that unlike the studies that introduce biaxial strain, the present method of interphase strain has little dependence of substrates. Super-tetragonal films such as PT (I) can also be successfully obtained on other lattice-mismatched substrates, such as inexpensive $LaAlO_3$ or sapphire, indicating it is distinctly irrelevant to substrate biaxial strain from both Poisson and electrostriction effects (Detailed discussion in Table S1 and fig. S5 and S6).

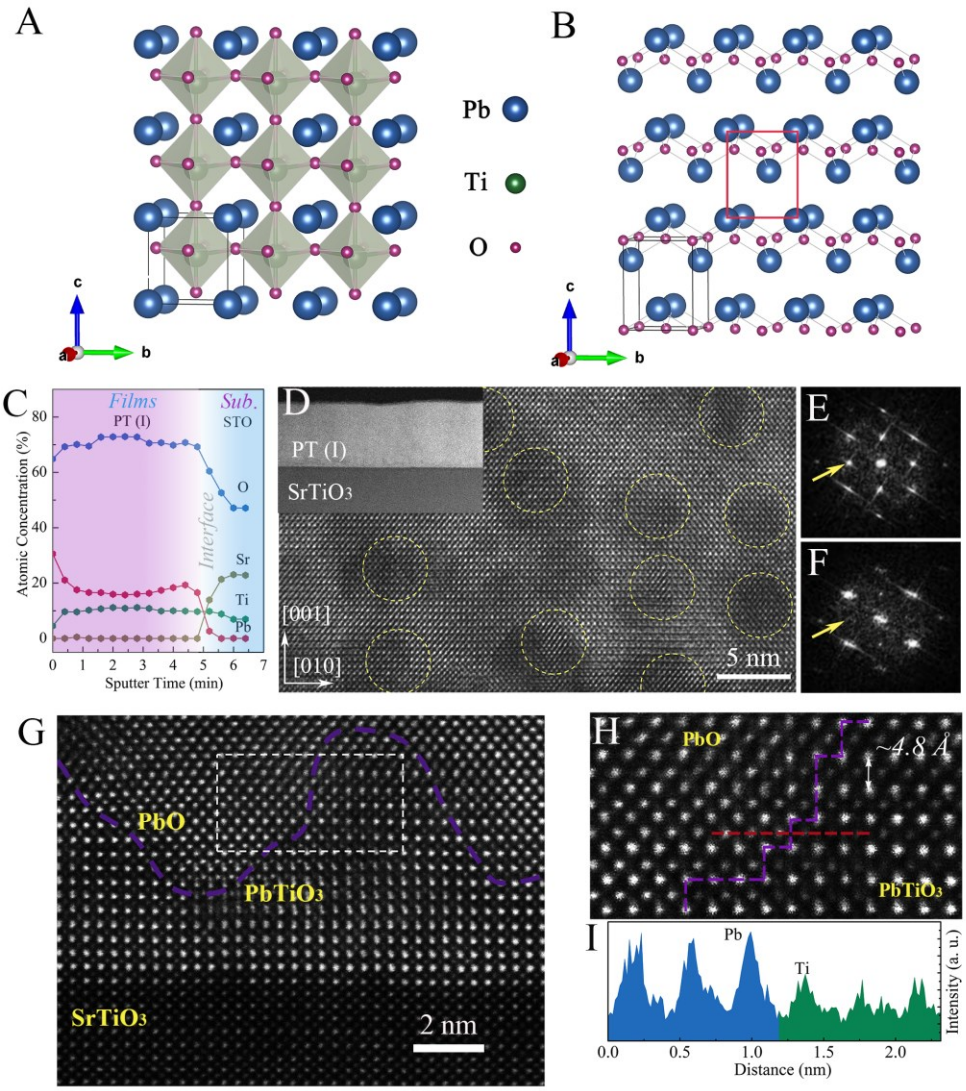

Fig. 2. Atomic resolution microstructure of epitaxial composite films. (**A**) Crystalline structure of $PbTiO_3$. (**B**) Crystalline structure of PbO. (**C**) Atomic concentration depth analysis by Auger electron spectroscopy of the PT (I) thin films. (**D**) High-resolution transmission electron microscopy image along the *a*-

axis of the PT (I) thin films, which underpins the epitaxial growth and a single set of tetragonal lattice parameters. The inset displays the low-magnification cross-section image. The regions indicated by the yellow dashed circles represent PbO. (**E**) The fast Fourier transform (FFT) pattern taken from the regions surrounding the yellow dashed circles, featuring the $PbTiO_3$

structure. (**F**) The FFT pattern taken from a typical example of the regions marked by yellow dashed circles, indicating the PbO structure. (**G**) HAADF-STEM image of the heteroepitaxial interface between $PbTiO_3$ and PbO viewed along the *a* axis of the PT (I) thin film. It also demonstrates that $PbTiO_3$ firstly grew on the substrate. The detailed discussion of the interface between film and substrate is in fig. S6. (**H**) Enlarged view of the white rectangle in **G**, verifying that $PbTiO_3$ and PbO have the same lattice parameters. (**I**) Intensity profile along the red dashed line in **H**, directly revealing the transition from Ti to Pb.

To further characterize the interface between $PbTiO_3$ and PbO, we carried out first-principles calculations. To model this system we used a number of infinitely extended layers of $PbTiO_3$ matched to an equal number of infinitely extended layers of PbO for four possible sets of planes: (100), (110), (101), and (001). For the (100) case we did this for groups that included 3, 5, and 7 layers containing Pb. For the (110) and (101) cases we used 6 and 10 layers (Fig. 3A). For the (001) case we used 3 and 5 layers. In all cases the atomic configurations were fully relaxed until the forces between atoms were below 0.01 eV/Å, and the stresses on the cell were below 0.01 GPa. As depicted in Fig. 3B, the calculations of *c*/*a* ratio, lattice parameters and displacement of Ti atom (δz_{Ti}) with respect to the center of the cage of surrounding Pb atoms are converged well with increasing number of layers. For the (100), (110), and (101) interfaces the *c*/*a* ratio is around 1.22, in excellent agreement with the experimental result; even for the (001) interface, *c*/*a* is almost 1.2. The results theoretically prove the particular concept of interphase strain.

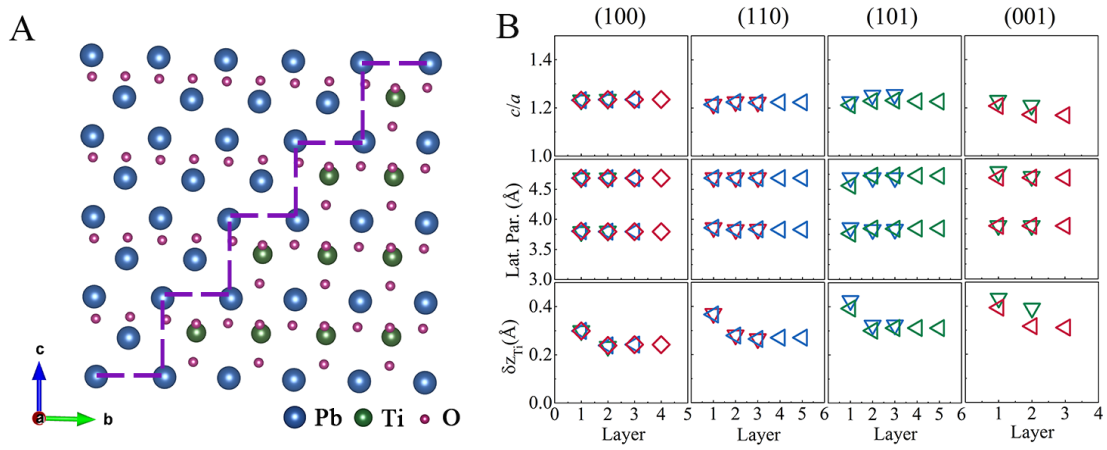

Fig. 3. Calculations of $PbTiO_3$/PbO interfaces. (**A**) Example of $PbTiO_3$/PbO system in our calculations (periodic boundary conditions apply): $PbTiO_3$/PbO (101) interface (purple dashed line), viewed along the *a* axis. (**B**) Structural results of density-functional theory calculations of four different $PbTiO_3$/PbO interfaces. Top row: tetragonal *c*/*a* ratio; middle row: *c* and *a* lattice parameters; bottom row: spontaneous polarization δz_{Ti}.

A giant *c*/*a* ratio is normally associated with a large polarization in perovskite oxides. The ferroelectric hysteresis loops feature a remanent polarization (P_r) of PT (I) as large as 236.3 $\mu C/cm^2$ (Fig. 4A). Intriguingly, the present polarization of PT (I) is the highest one ever reported for ferroelectrics (Fig. 4B) (*10*,*23*-*25*). For example, it is 1.8 times as large as that of the tetragonal-like $BiFeO_3$ epitaxial thin films (130 $\mu C/cm^2$) and 3.4 times of that of the strained $BaTiO_3$ thin films (70 $\mu C/cm^2$) (*10*,*25*). It is also much larger than those calculated spontaneous polarization values of Pb or Bi based perovskites with large *c*/*a* ratio, such as $PbVO_3$ (179 $\mu C/cm^2$) and $BiCoO_3$ (152 $\mu C/cm^2$) (*26*). The nature of the giant polarization can also be directly revealed by the large δz_{Ti} as displayed in fig. S6 (*17*,*27*). In PT (I), the STEM result for the δz_{Ti} value is 0.474 Å, almost three times as for bulk $PbTiO_3$ (0.162 Å) (*28*), which directly reveals the crystallographic character of giant spontaneous polarization. Furthermore, the δz_{Ti} value of first-principles calculations in some cases at the interface gets close to the one found experimentally (Fig. 3B). Hence, there is very likely a strong electrostatic interaction at the phase

boundary of the ferroelectric/paraelectric interfaces between $PbTiO_3$ and PbO (*29*), resulting in the strong polarization. In the PT (II) thin films a large P_r (129.6 μC/cm^2) was also observed (fig. S7). A linear correlation between P_r and c/a has been found in the top left inset of Fig. 4A. The ferroelectricity of PT (I) is supported by piezoelectric measurements (the bottom right inset of Fig. 4A). The relative yellow (1 μm square) and pink (3 μm square) contrasts indicate the upward (-10 V) and downward (+10 V) polarization states, respectively. The domain pattern after switching clearly underpins the intrinsic nature of ferroelectricity in PT (I). Local piezoresponse amplitude and phase curves demonstrate apparent ferroelectric switching (fig. S7).

Note that the existence of PbO contributes little to the polarization (fig. S8-S11), the PT (I) thin films show negligible leakage current (fig. S12), and the giant polarization phenomenon has been observed in abundant samples. The tilted hysteresis loop is suggested to be related to the continuous multilevel switching in such composite of ferroelectric $PbTiO_3$ and dielectric PbO. Similar phenomenon with multi-step polarization process be also caused by the switching hindering effect related to the ferroelastic-ferroelectric coupling (*30*). The facts of occasionally observed multi-step polarization process and the stable shape of the hysteresis loop as a function of temperature or frequency imply the intrinsic ferroelectricity of the present thin films, which is different to electrets (Detailed discussions in Supplementary Text, fig. S13-S16).

Temperature-dependent XRD was performed to determine the ferroelectric phase stability of the present films. As depicted in Fig. 4C, the ferroelectric phase of PT (I) is stable up to 725 °C, compared with the T_C (490 °C) of bulk $PbTiO_3$ (*20*). PT (I) exhibits the highest temperature for ferroelectric phase in all reported $PbTiO_3$ studies. According to the Landau-Ginzburg-Devonshire (LGD) theory (*17*), if the crystal structure could be more stable against temperature, its ferroelectric-to-paraelectric phase transition (~1000 °C) could be even higher in the PT(I) thin

films which have giant *c*/*a* and polarization. The cyclic curves reveal a stable tetragonal structure for PT (I) if temperatures up to 650 °C (fig. S18B). In the tetragonal phase, the *c* axis of PT (I) features a similar positive thermal expansion to that of PbO, which indicates that PbO determines the thermal expansion of $PbTiO_3$ (Table S2). At temperatures higher than 725 °C, irreversible structural transformation occurs, in which the *c* axis of PT (I) collapses from the large value of 4.92 Å to the normal value of 3.98 Å in the PT (III). At the same time, the excess PbO is isolated from the lattice of $PbTiO_3$ as a second phase (fig. S19). A huge volume contraction (19 %) occurs at the structure collapse temperature in PT (I), which has never been observed in negative thermal expansion materials. As a comparison, the largest volume contraction ever reported is 2.6 % for $BiNiO_3$ and it is 1 % for $LaCu_3Fe_4O_{12}$ (*31*). Such huge volume contraction in the present PT (I) should be originated from the role of spontaneous volume ferroelectrostriction (SVFS) (*31*), in which giant spontaneous polarization will produce a large ferroelectric volume. Thus a large volume contraction occurs during the collapse process with the loss of ferroelectricity.

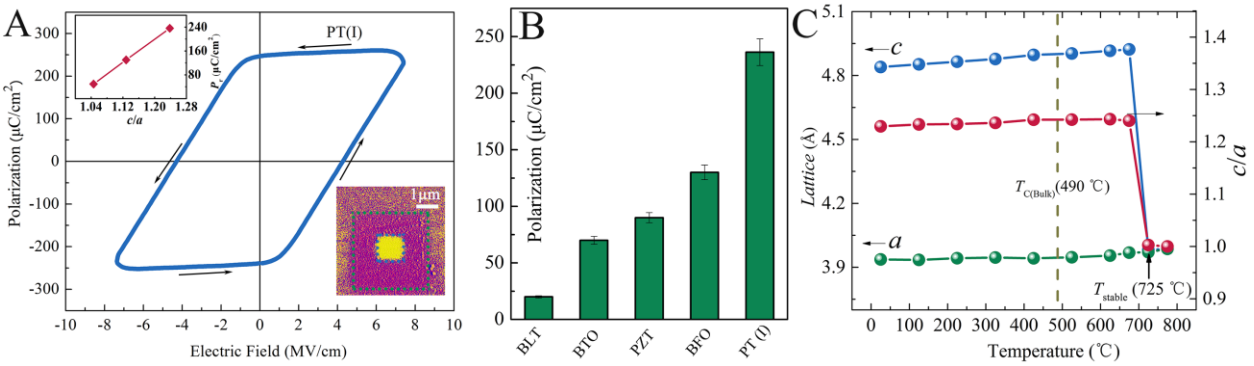

Fig. 4. Giant ferroelectric polarization and enhanced ferroelectric temperature in the PT (I) epitaxial composite films. (**A**) Ferroelectric hysteresis loop of the PT (I) thin films with a thickness of 129 nm grown on 0.7 wt % Nb-doped STO with Pt top electrode. The top left inset depicts the remanent polarization as a function of *c*/*a*. The bottom right inset displays out-of-

plane phase image after a box-in-box switching with a tip bias of ±10 V in the PT (I) thin films with a thickness of 38 nm by piezoresponse force microscopy. (**B**) Comparison of polarization of the present PT (I) thin films with the previously experimentally measured P_r in films from left to right: $Bi_{3.25}La_{0.75}Ti_3O_{12}$ (BLT) (*23*), strained $BaTiO_3$ (BTO) (*24*), unstrained $Pb(Zr_{0.2}Ti_{0.8})O_3$ (PZT) (*25*), and strained $BiFeO_3$ (BFO) (*10*). (**C**) Temperature dependence of lattice parameters and *c*/*a* of PT (I). The position of T_C of bulk $PbTiO_3$ is indicated by the dotted line for comparison.

In order to elucidate the mechanism of the giant ferroelectric polarization in PT (I), we have studied its electronic hybridization using X-ray absorption spectroscopy (XAS). The electronic state of the 3*d* levels is highlighted in Fig. 5A. On the basis of crystal field theory, the fivefold degenerated 3*d* level splits into doublet e_g and triplet t_{2g} levels in the octahedral symmetry (*32*). In the tetragonal symmetry, e_g (t_{2g}) levels should be split into d_{x2-y2} and d_{3z2-r2} (d_{xy} and $d_{yz,\ zx}$) orbitals. A larger *c*/*a* would generate a larger splitting. For tetragonal ferroelectrics, the Ti^{4+} transition metal ions shift along an apical direction, which brings in the higher *c*-axis orbital (d_{3z2-r2} and $d_{yz,\ zx}$) and lower in-plane orbital (d_{x2-y2} and d_{xy}). Hence the splitting between d_{x2-y2} and d_{3z2-r2} (d_{xy} and $d_{yz,\ zx}$) orbitals will be weakened. The splitting of L_3 e_g peaks becomes smaller from PT (III) to PT (I) as provided in Fig. 5B. Both the energy of d_{x2-y2} and d_{3z2-r2} orbitals decreases with increasing *c*/*a*, while the ΔE (d_{x2-y2}-d_{3z2-r2}) also reduces from 0.66 eV to 0.28 eV (Fig. 5C). As discussed above, the weakened splitting of e_g in PT (I) with enhanced *c*/*a* indicates larger Ti^{4+} distortion (off-center displacement), resulting in the giant ferroelectric polarization. Furthermore, both the decrease in the energy difference between the two main peaks of the L_3 or L_2 edges and the lower intensity of L_3 t_{2g} or L_2 t_{2g} indicate the enhanced ionic distortion and the existence of Ti^{3+} ions in the PT (I) thin films. This is in good agreement with O *K*-edge XAS and XPS (fig. S20 and S21). The existence of Ti^{3+} ions would cause additional imperfection in the crystal with increasing distortions and also enhance the polarization (fig. S21).

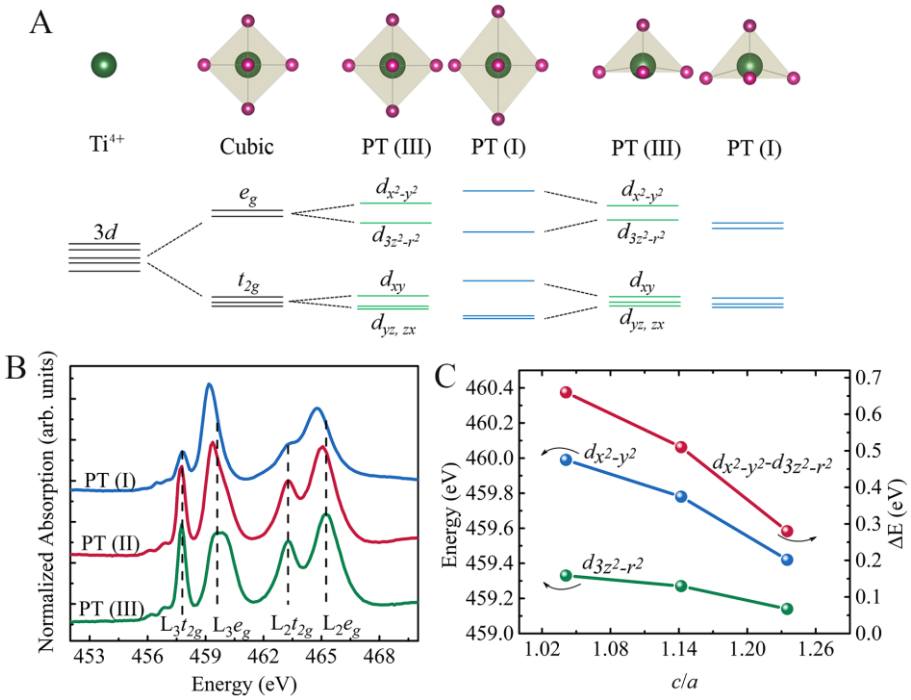

Fig. 5 Electronic hybridization analysis. (**A**) Schematic diagram of local structures of the transition metal Ti oxide, and the 3*d* level splits in the spherical, oxygen octahedral, tetragonal and polar tetragonal site symmetries for the PT (I) and PT (III) thin films. (**B**) Ti $L_{2,3}$-edge X-ray absorption spectroscopy measurements of PT (I), PT (II), and PT (III) thin films. (**C**) Energy of $d_{x2\text{-}y2}$ and $d_{3z2\text{-}r2}$ peaks of L_3 e_g orbitals as a function of *c*/*a*.

In summary, this study unveils the unprecedented giant remanent polarization (236.3 μC/cm^2) and much enhanced stable temperature (725 °C) in super-tetragonal $PbTiO_3$ ferroelectrics through the process of interphase strain. The STEM results revealed the intrinsic microstructure of heteroepitaxial interphase between $PbTiO_3$ and PbO. The giant polarization was confirmed by both the STEM and XAS measurements, which originates from large off-center ionic displacements. The density-functional theory calculations verify the large *c*/*a* ratios for various $PbTiO_3$/PbO interfaces that are very similar to the ones obtained experimentally. We conclude by stressing some advantages of the present method, which could create a new pathway for material design: i. The interphase strain can provide not only isotropic tensile strain but also isotropic

compressive strain; ii. The level of strain can be modulated by adjusting the composition (fig. S22); iii. The achievement of strain in thin films can be free from the choice of substrates.

References and Notes:

1. D. G. Schlom, L. Q. Chen, C. J. Fennie, V. Gopalan, Elastic strain engineering of ferroic oxides. *MRS Bull.* **39**, 118-130 (2014).
2. J. P. Locquet, J. Perret, J. Fompeyrine, E. Mächler, J. W. Seo, G. V. Tendeloo, Doubling the critical temperature of $La_{1.9}Sr_{0.1}CuO_4$ using epitaxial strain. *Nature* **394**, 453-456 (1998).
3 . R. von Helmolt, J. Wecker, B. Holzapfel, L. Schultz, K. Samwe, Giant negative magnetoresistance in perovskitelike $La_{2/3}Ba_{1/3}$ MnO_x ferromagnetic films. *Phys. Rev. Lett.* **71**, 2331 (1993).
4. H. Béa, B. Dupé, S. Fusil, R. Mattana, E. Jacquet, B. Warot-Fonrose, F. Wilhelm, A. Rogalev, S. Petit, V. Cros, A. Anane, F. Petroff, K. Bouzehouane, G. Geneste, B. Dkhil, S. Lisenkov, I. Ponomareva, L. Bellaiche, M. Bibes, A. Barthélémy, Evidence for room-temperature multiferroicity in a compound with a giant axial ratio. *Phys. Rev. Lett.* **102**, 217603 (2009).
5. A. K. Yadav, C. T. Nelson, S. L. Hsu, Z. Hong, J. D. Clarkson, C. M. Schlepütz, A. R. Damodaran, P. Shafer, E. Arenholz, L. R. Dedon, D. Chen, A. Vishwanath, A. M. Minor, L. Q. Chen, J. F. Scott, L. W. Martin, R. Ramesh, Observation of polar vortices in oxide superlattices. *Nature* **530**, 198-201 (2016).
6. Y. L. Tang, Y. L. Zhu, X. L. Ma, A. Y. Borisevich, A. N. Morozovska, E. A. Eliseev, W. Y. Wang, Y. J. Wang, Y. B. Xu, Z. D. Zhang, S. J. Pennycook, Observation of a periodic array of flux-closure quadrants in strained ferroelectric $PbTiO_3$ films. *Science* **348**, 547-551 (2015).
7. P. Zubko, J. C. Wojdeł, M. Hadjimichael, S. Fernandez-Pena, A. Sené, I. Luk'yanchuk, J.-M. Triscone, J. Íñiguez, Negative capacitance in multidomain ferroelectric superlattices. *Nature* **534**, 524-528 (2016).
8. D. Lee, H. Lu, Y. Gu, S.-Y. Choi, S.-D. Li, S. Ryu, T. R. Paudel, K. Song, E. Mikheev, S. Lee, S. Stemmer, D. A. Tenne, S. H. Oh, E. Y. Tsymbal, X. Wu, L.-Q. Chen, A. Gruverman, C. B. Eom, Emergence of room-temperature ferroelectricity at reduced dimensions. *Science* **349**, 1314-1317 (2015).

9. R. J. Zeches, M. D. Rossell, J. X. Zhang, A. J. Hatt, Q. He, C.-H. Yang, A. Kumar, C. H. Wang, A. Melville, C. Adamo, G. Sheng, Y.-H. Chu, J. F. Ihlefeld, R. Erni, C. Ederer, V. Gopalan, L. Q. Chen, D. G. Schlom, N. A. Spaldin, L. W. Martin, R. Ramesh, A strain-driven morphotropic phase boundary in $BiFeO_3$. *Science* **326**, 977-980 (2009).
10. J. X. Zhang, Q. He, M. Trassin, W. Luo, D. Yi, M. D. Rossell, P. Yu, L. You, C. H. Wang, C. Y. Kuo, J. T. Heron, Z. Hu, R. J. Zeches, H. J. Lin, A. Tanaka, C. T. Chen, L. H. Tjeng, Y.-H. Chu, R. Ramesh, Microscopic origin of the giant ferroelectric polarization in tetragonal-like $BiFeO_3$. *Phys. Rev. Lett.* **107**, 147602 (2011).
11. A. A. Belik, M. Azuma, T. Saito, Y. Shimakawa, M. Takano, Crystallographic features and tetragonal phase stability of $PbVO_3$, a new member of $PbTiO_3$ family. *Chem. Mater.* **17**, 269-273 (2005).
12. A. A. Belik, S. Iikubo, K. Kodama, N. Igawa , S. Shamoto, S. Niitaka, M. Azuma, Y. Shimakawa, M. Takano, F. Izumi, E. Takayama-Muromachi, Neutron powder diffraction study on the crystal and magnetic structures of $BiCoO_3$. *Chem. Mater.* **18**, (798-803) (2006).
13. J. Wang, J. B. Neaton, H. Zheng, V. Nagarajan, S. B. Ogale, B. Liu, D. Viehland, V. Vaithyanathan, D. G. Schlom, U. V. Waghmare, N. A. Spaldin, K. M. Rabe, M. Wuttig, R. Ramesh, Epitaxial $BiFeO_3$ multiferroic thin film heterostructures. *Science* **299**, 1719-1722 (2003).
14. J. H. Lee, L. Fang, E. Vlahos, X. Ke, Y. W. Jung, L. F. Kourkoutis, J.-W. Kim, P. J. Ryan, T. Heeg, M. Roeckerath, V. Goian, M. Bernhagen, R. Uecker, P. C. Hammel, K. M. Rabe, S. Kamba, J. Schubert, J. W. Freeland, D. A. Muller, C. J. Fennie, P. Schiffer, V. Gopalan, E. Johnston-Halperin , D. G. Schlom, A strong ferroelectric ferromagnet created by means of spin-lattice coupling. *Nature* **466**, 954-958 (2010).
15. S. Tinte, K. M. Rabe, D. Vanderbilt, Anomalous enhancement of tetragonality in $PbTiO_3$ induced by negative pressure. *Phys. Rev. B* **68**, 144105 (2003).
16. A. R. Damodaran, E. Breckenfeld, Z. Chen, S. Lee, L. W. Martin, Enhancement of ferroelectric Curie temperature in $BaTiO_3$ films via strain-induced defect dipole alignment. *Adv. Mater.* **26**, 6341-6347 (2014).
17. J. Wang, B. Wylie-van Eerd, T. Sluka, C. Sandu, M. Cantoni, X.-K. Wei, A. Kvasov, L. J. McGilly, P. Gemeiner, B. Dkhil, A. Tagantsev, J. Trodahl, N. Setter, Negative-pressure-induced enhancement in a freestanding ferroelectric. *Nat. Mater.* **14**, 985-990 (2015).

18. A. Kvasov, L. J. McGilly, J. Wang, Z. Shi, C. S. Sandu, T. Sluka, A. K. Tagantsev, N. Setter, Piezoelectric enhancement under negative pressure. *Nat. Commun.***7**, 12136 (2016).

19. C. Lichtensteiger, J. M. Triscone, J. Junquera, P. Ghosez, Ferroelectricity and tetragonality in ultrathin $PbTiO_3$ films. *Phys. Rev. Lett.* **94**, 047603 (2005).

20. S. A. Mabud, A. M. Glazer, Lattice parameters and birefringence in $PbTiO_3$ single crystals. *J. Appl. Cryst.* **12**, 49-53 (1979).

21. H. E. Swanson, R. K. Fuyat, *Natl. Bur. Stand. (US) Circ.* **539**, (1953).

22. G. Catalan, A. Lubk, A. H. G. Vlooswijk, E. Snoeck, C. Magen, A. Janssens, G. Rispens, G. Rijnders, D. H. A. Blank, B. Noheda, Flexoelectric rotation of polarization in ferroelectric thin films. *Nat. Mater.* **10**, 963-967 (2011).

23. B. H. Park, B. S. Kang, S. D. Bu, T. W. Noh, J. Lee, W. Jo, Lanthanum-substituted bismuth titanate for use in non-volatile memories. *Nature* **401**, 682-684 (1999).

24. K. J. Choi, M. Biegalski, Y. L. Li, A. Sharan, J. Schubert, R. Uecker, P. Reiche, Y. B. Chen, X. Q. Pan, V. Gopalan, L.-Q. Chen, D. G. Schlom, C. B. Eom, Enhancement of ferroelectricity in strained $BaTiO_3$ thin films. *Science* **306**, 1005-1009 (2004).

25. V. Nagarajan, I. G. Jenkins, S. P. Alpay, H. Li, S. Aggarwal, L. Salamanca-Riba, A. L. Roytburd, R. Ramesh, Thickness dependence of structural and electrical properties in epitaxial lead zirconate titanate films. *J. Appl. Phys.* **86**, 595-602 (1999).

26. Y. Uratani, T. Shishidou, F. Ishii, T. Oguchi, First-principles predictions of giant electric polarization. *Jpn. J. Appl. Phys.* **44**, 7130-7133 (2005).

27. S. C. Abrahams, S. K. Kurtz, P. B. Jamieson, Atomic displacement relationship to Curie temperature and spontaneous polarization in displacive ferroelectrics. *Phys. Rev.* **172**, 551-553 (1968).

28. A. M. Glazer, S. A. Mabud, Powder profile refinement of lead zirconate titanate at several temperatures. II. Pure $PbTiO_3$. *Acta Cryst.* **B34**, 1065-1070 (1978).

29. E. Khestanova, N. Dix, I. Fina, M. Scigaj, J. M. Rebled, C. Magén, S. Estradé, F. Peiró, G. Herranz, J. Fontcuberta, F. Sánchez, Untangling electrostatic and strain effects on the polarization of ferroelectric superlattices. *Adv. Funct. Mater.* **26**, 6446-6453(2016).

30. P. Gao, J. Britson, J. R. Jokisaari, C. T. Nelson, S. H. Baek, Y. Wang, C. B. Eom, L. Q. Chen, X. Pan, Atomic-scale mechanisms of ferroelastic domain-wall-mediated ferroelectric switching. *Nat. Commun.* **4**, 2791 (2013).

31. J. Chen, L. Hu, J. X. Deng, X. R. Xing Negative thermal expansion in functional materials: controllable thermal expansion by chemical modifications. *Chem. Soc. Rev.* **44**, 3522-3567 (2015).
32. K.-T. Ko, M. H. Jung, Q. He, J. H. Lee, C. S. Woo, K. Chu, J. Seidel, B.-G. Jeon, Y. Seok Oh, K. H. Kim, W.-I Liang, H.-J. Chen, Y.-H. Chu, Y. H. Jeong, R. Ramesh, J.-H. Park, C.-H. Yang, Concurrent transition of ferroelectric and magnetic ordering near room temperature. *Nat. Commun.* **2**, 567 (2011).

Acknowledgments: This work was supported by the National Natural Science Foundation of China (Grant Nos. 91422301, 21231001, 21590793), the Changjiang Young Scholars Award, the National Program for Support of Top-notch Young Professionals, and the Fundamental Research Funds for the Central Universities, China (Grant No. FRF-TP-14-012C1). Use of the Beijing Synchrotron Radiation Facility (1W1A and 4B9B beamlines, China) and the Shanghai Synchrotron Radiation Facility (BL14B1 beamline, China) of the Chinese Academy of Sciences. O.D. acknowledges funding from the Israel Science Foundation through Grants No. 1814/14 and No. 2143/14. We thank Qi Liu, Panyang Hang, and Yuzhen Cai for the preparation of electrodes by photolithography at University of Science and Technology Beijing, Qingxiao Wang and Zifan Che for the preparation of STEM samples by focused ion beam at University of Texas at Dallas, and Dongxing Zheng for the analysis of PFM at Tianjin University.

Supplementary Materials:

Materials and Methods

Figures S1-S22

Table S1-S2

References (33-54)